JOURNAL OF GEOPHYSICAL RESEARCH, VOL. 105, NO. A1, PAGES 317–328, JANUARY 1, 2000

Magnetotail waveguide: Fast and Alfvén waves in the plasma sheet boundary layer and lobe

W. Allan
National Institute of Water and Atmospheric Research, Wellington, New Zealand

Andrew N. Wright
Mathematical Institute, University of St. Andrews, St. Andrews, Scotland

Abstract. Numerical simulations of MHD wave propagation and coupling in a realistic magnetotail are presented. Fast mode waves are observed to disperse and couple resonantly to Alfvén waves over a broad layer rather than on an isolated field line. Indeed, the layer is likely to be so broad as to include the entire tail lobe as well as the plasma sheet boundary layer (PSBL). It appears that small k_y modes (where k_y is the cross-tail wave number) will provide the most efficient coupling as they will tend to propagate along the magnetotail field lines rather than across them and out of the tail boundaries. (Moreover, it is only small k_y fast modes that will be able to penetrate the lobe.) Alfvén waves in the PSBL are shown to phase mix rapidly resulting in strong field-aligned currents with an equatorward phase motion. These properties are in agreement with observations of optical auroral emissions. The lobe Alfvén waves do not phase mix, and are not expected to excite optical emissions. They may, however, provide a significant ponderomotive force and could account for the transport of oxygen ions from the ionosphere into the distant tail lobes.

1. Introduction

Hydromagnetic waveguides have been studied by theorists in a space plasma context for over three decades. Magnetotail work dates back to *McClay and Radoski* [1967], and increasing detail has been added by subsequent workers (see the review by *Allan and Wright* [1998, hereinafter AW]. The magnetotail is known to support waves of millihertz frequencies [*Herron*, 1967], and normal mode calculations confirm that the natural waveguide frequencies are of this order.

More recently, attention has focused upon how waves in the tail will couple [*Goertz and Smith*, 1989; *Liu et al.*, 1995; AW; *Wright et al.*, 1999]. The good agreement between a number of features seen in optical auroral data [*Samson et al.*, 1991; *Xu et al.*, 1993] and the predictions of theory have enhanced our knowledge of magnetotail structure and dynamics. For example, substorms can be viewed as a source of fast MHD waves which are ducted by the plasma sheet [*Elphinstone et al.*, 1995]. These fast mode disturbances can couple to Alfvén waves and may be correlated with optical auroral emissions [*Liu et al.*, 1995; *Wright et al.*, 1999].

The present paper extends the theory developed by AW and *Wright et al.* [1999] by including realistic density distributions across the tail (in the z coordinate) and by allowing for density variation along the tail (in the x coordinate). We find that a general fast mode source in the tail will couple a (probably small) fraction of its energy into Alfvén waves in the PSBL, and, perhaps surprisingly, the tail lobe. The PSBL Alfvén waves phase mix to generate large field-aligned currents with an equatorward phase motion that are thought to be associated with equatorward moving auroral emissions [e.g., *Samson et al.*, 1992]. The lobe is approximately uniform, so the Alfvén waves here do not phase mix, and remain essentially as plane waves. Strong field-aligned currents are absent in the lobe but during reflection from the ionosphere the Alfvén waves have a local standing structure which may generate a ponderomotive force that does not time average to zero. These lobe Alfvén waves could be important for accelerating oxygen ions into the lobe, although they are unlikely to produce auroral emissions.

We suggest that a suitable driver of waves in the magnetotail could be the ejection of plasmoids associated with substorms and the reconfiguration of the tail to a new equilibrium. A simple estimate of the amplitude of wave fields and currents that result show these could play an important role in generating auroral optical emissions and may accelerate plasma into the tail.

2. Model Structure

As discussed by AW, our hydromagnetic box model magnetotail waveguide has a magnetic field which ex-

Paper number 1999JA900425.
0148-0227/00/1999JA900425$09.00

tends parallel to the waveguide axis rather than being across the waveguide. The coordinate x extends from a position in the tail at $x = 0$ to $x = x_E$, the "Earth." The coordinate z extends across the waveguide from $z = -z_M$ at the southern magnetopause to $z = z_M$ at the northern magnetopause. Variation in the third dimension y is represented by a single Fourier component. All distances are normalized by z_M below.

The magnetic field $\boldsymbol{B} = B_0\hat{\mathbf{x}}$ is uniform. Plasma mass density is chosen to vary with z across the northern half of the waveguide in such a way as to give the following piecewise continuous variation of Alfvén speed with z:

$$V_A(z) = \begin{cases} v_1 + c_1 z^{p_1} & 0 \le z < z_1/2 \\ v_2 - c_1(z_1 - z)^{p_1} & z_1/2 \le z < z_1 \\ v_2 & z_1 \le z < z_2 \\ v_2 + c_2(z - z_2)^{p_2} & z > z_2, \end{cases} \tag{1}$$

where $c_1 = \frac{1}{2}(v_2 - v_1)(2/z_1)^{p_1}$ and $c_2 = (v_3 - v_2)/(1 - z_2)^{p_2}$. The central plane of the magnetotail is at $z = 0$ where $V_A = v_1$. The CPS/PSBL lies between 0 and z_1, with the maximum value of dV_A/dz occurring at $z_1/2$. The northern lobe lies between z_1 and z_2, and has a constant $V_A = v_2$. The plasma mantle lies between z_2 and the magnetopause at $z = z_M$, where $V_A = v_3$. The profile (1) has a continuous first derivative with respect to z, and the parameters p_1 and p_2 are chosen to give required values of dV_A/dz in the PSBL and mantle. The southern half of the magnetotail is a mirror image of the northern half reflected in $z = 0$.

To allow for variation in the x direction, (1) can be multiplied by the following function:

$$f(x) = (f_0)^{x^{p_3}}, \tag{2}$$

where f_0 and p_3 are chosen constants.

Since our primary concern is to study the propagation of fast waves and how they couple to Alfvén waves, we have adopted a cold plasma equilibrium model. Not only does this remove the slow mode from our consideration (which we expect would be strongly Landau damped in reality) but it reduces the number of governing equations to be integrated and increases our computational efficiency. Of course, the magnetotail is not a cold plasma, and β is certainly greater than 1 in the plasma sheet. However, since the fast mode propagates at a speed $c_f = (V_A^2 + c_s^2)^{1/2}$ (where c_s is the sound speed) it is surprisingly insensitive to the details of how our equilibrium satisfies total pressure balance across the tail. For example, given the equilibrium density variation and total pressure we can calculate the fast speed in the center of the plasma sheet ($z = 0$) for the two extreme cases of $\beta(z = 0) = \infty$ (i.e., $B(0) = 0$) and $\beta(z = 0) = 0$ (no plasma pressure at $z = 0$). The fast speed in these two limits differs by less than 10% (for $\gamma = 5/3$). Thus we expect our model to provide a realistic propagation speed for the fast mode, and the fast eigenfrequencies of our tail should correspond closely with those of a warm magnetotail waveguide. Our assumed uniformity of the equilibrium field strength will certainly affect the Alfven frequencies in our model. However, *Pulkkinen et al.* [1996] note that the field strength is fairly uniform across the PSBL and begins to decrease on entering the plasma sheet. Thus our assumption of a uniform magnetic field is a reasonable approximation in the PSBL, and we should excite Alfvén waves there with realistic frequencies.

We solve the same set of linearized first-order ideal hydromagnetic equations in the waveguide as given in (3)–(7) of AW. Again, the velocity u_y is chosen to have a separable y variation of $\sin(k_y y)$, with $u_y = 0$ at the y boundaries of the waveguide. The other velocity and magnetic field components have y variations consistent with this.

The hydromagnetic equations are normalized using z_M as the unit of distance, and z_M/v_2 as the unit of time, where v_2 is the lobe Alfvén speed. Velocities are normalized using v_2, magnetic fields using B_0, and densities using $B_0^2/\mu_0 v_2^2$. From now on all quantities quoted will be normalized.

Boundaries are chosen to be perfectly reflecting at the magnetopause ($u_z(z = \pm z_M) = 0$) and at the "earthward" end of the box ($x = x_E$), the latter crudely representing the high-latitude ionosphere. Symmetry boundary conditions are applied at the $x = 0$ end of the waveguide ($\partial u_z/\partial x = 0$) and also in the center plane $z = 0$ ($u_z = 0$, except during the initial driving phase).

Waves in the guide are stimulated by a compressional disturbance in u_z occurring along the $z = 0$ line over the range $x = 0$ to x_d (where x_d is short compared with x_E) and for a time t_d short compared with the minimum Alfvén transit time to x_E. The form of the disturbance is

$$u_z \propto \cos(\pi t/t_d)[1 - \cos(2\pi t/t_d)]^2[1 + \cos(\pi x/x_d)] \tag{3}$$

for $0 < t \le t_d$, with $u_z = 0$ for $t > t_d$. This imposed velocity at $z = 0$ corresponds to a positive displacement at $z = 0^+$, and a negative displacement at $z = 0^-$. Note that there was a typographical error in (8) of AW, the square given in (3) above being omitted.

As discussed by AW, the phase and group velocity properties of the uncoupled ($k_y = 0$) WKB solutions to the waveguide problem are useful for interpreting the coupled wave results. The present case has more complicated behavior than that in AW because of the detailed internal structure of the waveguide. We consider two parameter choices for the z variation of Alfvén speed in (1). The first, referred to as Model A, has the parameters $v_1 = 0.25$, $v_2 = 1$, $v_3 = 0.5$, $z_1 = 0.2$, $z_2 = 0.8$, $p_1 = 3$, and $p_2 = 3$. The second, referred to as Model B, has $v_1 = 0.2$, $z_1 = 0.25$, $p_1 = 5$, and the other parameters the same as Model A.

Note that Models A and B have no x variation. We will also consider Model C, which has the Model A z variation multiplied by $f(x)$ from (2) with $f_0 = 2$ and $p_3 = 3$. Figures 1a and 1b show the z variations of V_A in Models A and B, and Figure 1c shows the x variation of V_A in Model C at $z = 0.5$. Note that Model B has a thicker CPS and thinner PSBL than Model A. The function $f(x)$ is chosen so that V_A increases rapidly near the Earth to twice the value at $x = 0$.

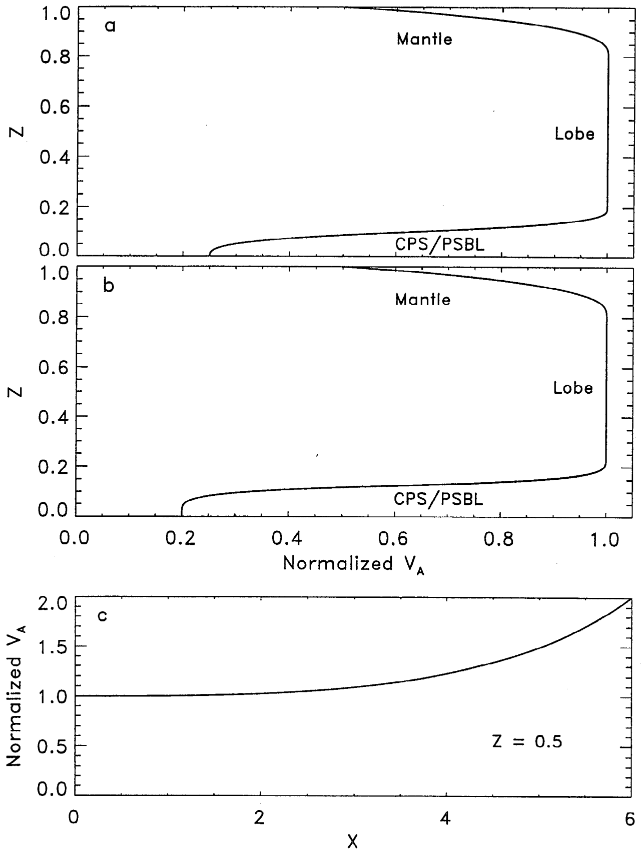

Figure 1. The variation of Alfvén speed with z in (a) Model A and (b) Model B. (c) Model C has the Alfvén variation with z shown in Figure 1a, but also a variation with x (equation (2)) as given in Figure 1c for $z = 0.5$.

The driver for Models A and C uses the values $t_d = 1$ and $x_d = 0.48$ in (3), while the driver for Model B uses $t_d = 1$ and $x_d = 0.24$. The choice of these parameter values is discussed in section 5.4.

In Figure 2 the dispersion and group velocity diagrams are given for Model A. In Figure 2a the solid curves show the waveguide mode parallel dispersion relations (frequency ω versus $k_\parallel \equiv k_x$) for the fundamental ($n = 1$) and second harmonic ($n = 2$) modes in z when $k_y = 0$. These curves were calculated using a shooting method, with boundary conditions $u_z = 0$ at $z = 0, \pm 1$. A mode with wavenumber $k_\parallel$ has a parallel phase velocity given by $V_{p\parallel} = \omega/k_\parallel$. Each z position represents a different field line with a specific Alfvén speed. The dashed lines show the range of field-aligned Alfvén wave phase speeds for the model ($0.25 \leq \omega/k_\parallel \leq 1.0$). The dash-dot line shows in arbitrary units the $k_\parallel$ Fourier amplitude spectrum of the applied impulse (3) for $x_d = 0.48$. The solid lines in Figure 2b give the parallel group velocity $V_{g\parallel} = \partial\omega/\partial k_\parallel$. The $n = 1$ curve has a characteristic maximum at a relatively small value of $k_\parallel$, followed by a slow decrease to the asymptotic value for infinite $k_\parallel$, given by the dashed line ($V_A(z = 0) = 0.25$). The $n = 2$ curve has a broad maximum at a larger value of $k_\parallel$.

Figure 3 shows the dispersion and group velocity curves for Model B. In this case the third harmonic ($n = 3$) mode is also given. The dashed lines show the range of field-aligned Alfvén wave phase speeds for the model ($0.2 \leq \omega/k_\parallel \leq 1.0$). The dash-dot line shows in arbitrary units the $k_\parallel$ Fourier amplitude spectrum of the applied impulse for $x_d = 0.24$. The change in the CPS/PSBL parameters between Models A and B has a strong effect on the properties of the fast waveguide harmonics. These properties will be used later to interpret the numerical results obtained in the coupled case where k_y is not zero.

3. Numerical Solution

The ideal hydromagnetic equation system (3)–(7) of AW is integrated forward in time using the leapfrog-trapezoidal algorithm [*Zalesak*, 1979], which is second-order accurate in both space and time. We use a fixed time step equal to a fraction of the shortest Alfvén transit time across one cell of the grid. Different (constant) grid spacings are chosen in x and z, with a finer grid spacing in z as phase mixing in the z direction may ultimately develop some of the shortest spatial structures in the simulation, especially as we have chosen steep

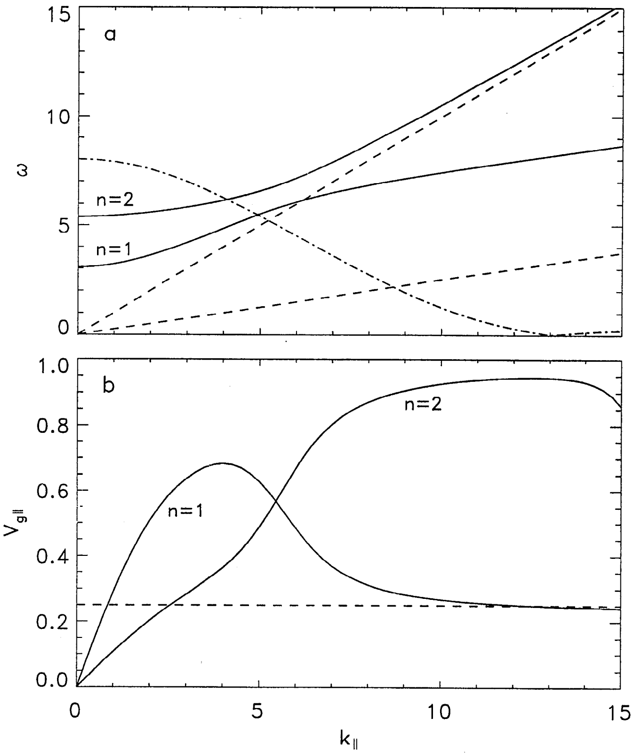

Figure 2. (a) The dispersion diagram for Model A. The two solid lines represent the first two ($k_y = 0$) fast harmonics, the dashed lines the extrema of the Alfvén continuum, and the dot-dashed line the amplitude spectrum (in arbitrary units) of the driver profile with $x_d = 0.48$. (b) The parallel group velocities of the fast modes. The dashed line represents the asymptotic group gelocity as $k_\parallel \to \infty$.

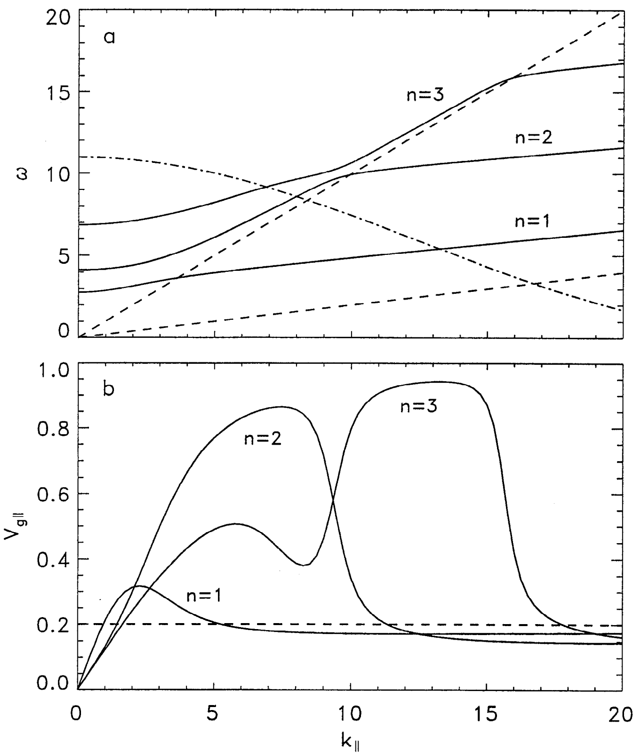

Figure 3. Similar format to Figure 2 but for Model B with the first three fast harmonics, and $x_d = 0.24$.

gradients in the PSBL region. The grid spacing in x must be at least fine enough to resolve the x structure of the initial perturbation (3) well. In Models A and C we choose $t_d = 1$ and $x_d = 0.48$, and in Model B we choose $t_d = 1$ and $x_d = 0.24$. Since wave propagation in the system is symmetrical about $z = 0$, we solve only in the region $z \geq 0$ and then reflect the solution in the line $z = 0$ to obtain the complete solution.

We choose $k_y = 1.3$ as the Fourier component perpendicular to the simulation plane allowing coupling between fast and Alfvén modes. If a half wavelength in y is taken as representing the width of the waveguide, then the width for $k_y = 1.3$ is ~2.4. This is consistent with the elliptical shape of the magnetotail cross section described by *Yamamoto et al.* [1994]. This fairly realistic value of k_y gives significantly stronger coupling between fast and Alfvén modes than in AW.

In all runs we took the time step to be 1/5 of the shortest transit time between two adjacent grid points. The final configurations used had 1000 grid points between $z = 0$ and 1 for Models A and C, and 2000 grid points in z for Model B. The length of the box x_E was chosen to be 6 in normalized units, and 300 grid points were taken between $x = 0$ and x_E. The simulation was run for up to nine time units so that disturbances traveling in the PSBL region could reach the end of the box at x_E. The grid spacings in z are small enough to ensure that the smallest phase mixing length $L_{ph} = 2\pi/k_z$ at $t = 9$ is well resolved, where k_z is given by (8) in section 5.2.

The ratio of the wave energy in the box at $t = 9$ to the total injected energy was about 0.9995 in all cases. The maximum value of normalized $\nabla \cdot \mathbf{B}$ for all positions and times in the box was about 5×10^{-12}. These figures show that the simulation is working with adequate accuracy. Convergence toward the correct numerical solution is assessed using the ratio $\delta u/\text{mod}(u)$, where u is a given field component, δu is the difference between values of u for two successively increasing grid resolutions at the center of the (x, z) domain at time t, and mod(u) is the maximum modulus of u over the (x, z) domain at time t. For Model A, $\delta u_z/\text{mod}(u_z) = 2.6 \times 10^{-4}$ at $t = 9$ with 500 and 1000 grid points in z. For Model B, $\delta u_z/\text{mod}(u_z) = 3.5 \times 10^{-4}$ at $t = 9$ with 1000 and 2000 grid points in z. Thus the simulations have converged adequately in both cases.

4. Results

As in AW, we use energy densities derived from the field components of the uncoupled fast and Alfvén waves as approximate diagnostics of the coupled modes in the waveguide. The uncoupled ($k_y = 0$) fast and Alfvén mode energy densities E_F and E_A are given by

$$E_F = (\rho u_z^2 + b_x^2 + b_z^2)/2 \qquad (4)$$

$$E_A = (\rho u_y^2 + b_y^2)/2. \qquad (5)$$

We also use the diagnostic D_A defined by

$$D_A = u_y + b_y/\rho^{1/2} \qquad (6)$$

which is exactly zero when the (u_y, b_y) wave field is that of solely an Alfvén wave propagating parallel to $\boldsymbol{B}$. If there is an Alfvén wave propagating antiparallel to $\boldsymbol{B}$, or a mixture of waves, D_A will be nonzero. If the (u_y, b_y) perturbations are significantly non-Alfvénic, then D_A is nonzero. Note that because the coupling is stronger in the present case, we might expect diagnostics (4) and (5) to be somewhat less useful here. The diagnostic (6) should be a measure of this also. We will display the wave "amplitudes" $E_F^{1/2}$ and $E_A^{1/2}$, rather than E_F and E_A, as these allow more detail to be seen in contour plots, for example.

4.1. Model A

In Figure 4 we display contour plots of $E_F^{1/2}$ and $E_A^{1/2}$ for Model A at time $t = 6$ when disturbances traveling at the Alfvén speed in the lobe should just be reaching the ionosphere. Each contour plot is normalized to its own maximum value. Even with larger coupling between fast and Alfvén modes, the energy density diagnostics still clearly distinguish between the coupled modes. For the fast mode in Figure 3a, the largest energy density is below the PSBL. Significant energy density exists in the lobe and mantle, but overall energy propagation in this mode is at a group speed a good deal less than the Alfvén speed. As discussed by AW and *Wright* [1994], this is because dispersion in the waveguide means that Fourier components with

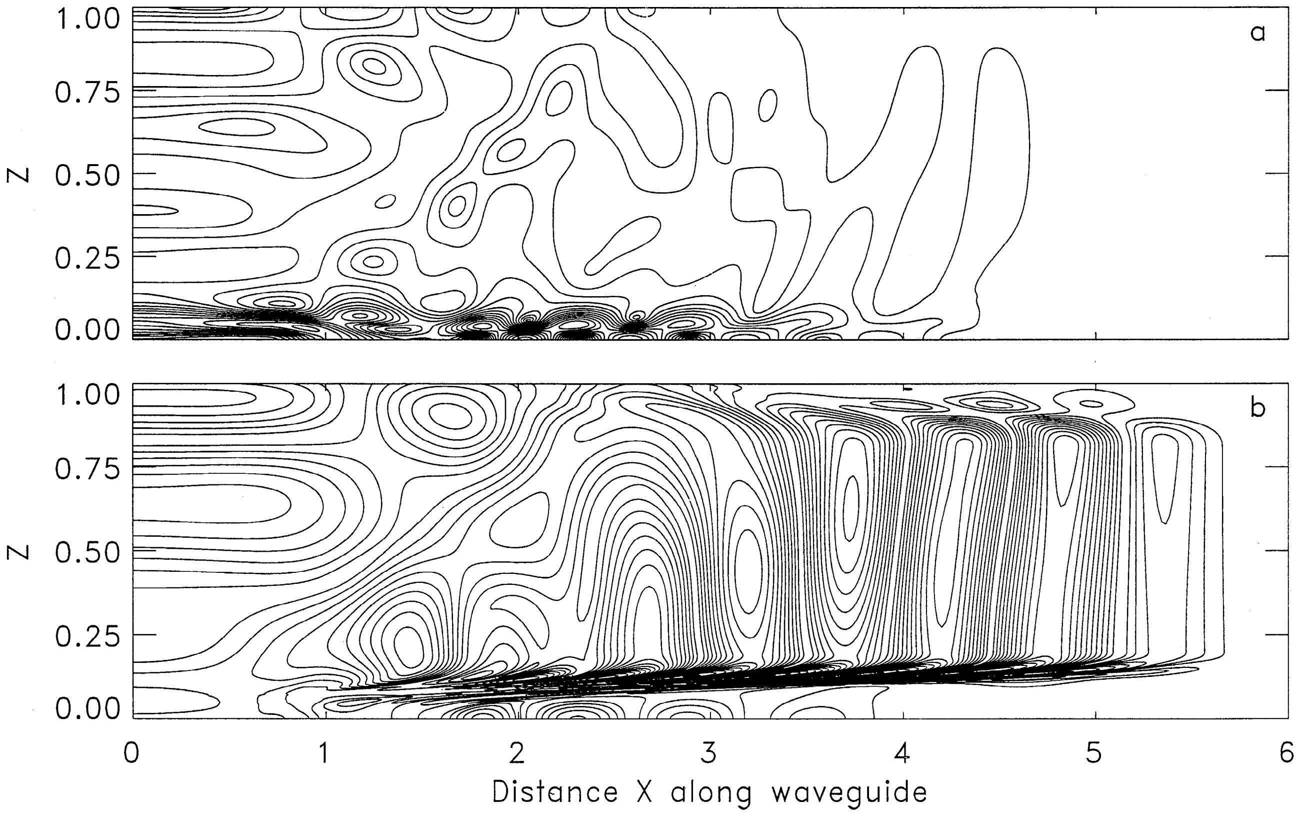

Figure 4. Contour plots of (a) fast and (b) Alfvén wave amplitudes at $t = 6.0$ for Model A ($t_d = 1.0$, $x_d = 0.48$, $k_y = 1.3$).

$k_{\|}/k_z > O(1)$ propagate down the waveguide quickly compared to components with $k_{\|}/k_z \ll 1$, which propagate mainly across the waveguide, and only very slowly along it.

The structure of $E_A^{1/2}$ in Figure 4b is interesting. Starting from ~2.5 units down the waveguide the development of essentially a plane Alfvén wave in the lobe is clear. The leading edge of this wave is just reaching the ionosphere at $t = 6$. The PSBL Alfvén wave is different, developing extremely tilted wavefronts very quickly, and leading us to expect strong phase mixing in the PSBL. The Alfvén wave in the mantle shows similar but much weaker behavior. Alfvén waves in the PSBL and below appear to be well short of reaching the ionosphere at this time.

To interpret the wave structure in Model A, we consider initially the case $k_y = 0$, so there will be no Alfvén waves excited in this run. Figure 5 shows fast wave snapshots for $t = 6$ at $z = 0.5$ in the center of the lobe and at $z = 0.125$ in the PSBL in this case. The $k_{\|}$ spectrum of the initial impulse in Figure 2 shows that we should not expect to see waves with noticeable amplitude for $k_{\|}$ greater than ~12, that is with $\lambda_{\|}$ less than ~0.5, and this appears to be so in Figure 5.

In Figure 2 the group velocity for the $n = 1$ mode has a relatively narrow peak at about 0.7, while the $n = 2$ mode has a broad peak with $V_{g\|}$ about 0.9 for $k_{\|} < 12$. At $z = 0.5$ in Figure 5 we might therefore expect to see waves of decreasing wavelength and amplitude extending close to $x = 6$, and this is indeed the case. Small-amplitude waves in fact extend exactly to $x = 6$. As discussed by *Brillouin* [1960], this is because there are always small amplitude "forerunners" of a wavepacket which can travel at the characteristic speed of the medium, that is $V_A = 1$ at $z = 0.5$. At $z = 0.125$ in Figure 5b, the local Alfvén speed is 0.842. No wave (even forerunners) propagating at or below $z \leq 0.125$ could reach further than $x = 5.05$ by $t = 6$. The waves at $z = 0.125$ extending nearly to $x = 6$ must therefore be refracted from larger z, in particular from the PSBL / lobe interface at $z = 0.2$ where $V_A \simeq 1$.

In Figure 6 we show the corresponding coupled "fast mode" waves for $k_y = 1.3$, and their associated "Alfvén" waves. It is clear that the coupling has modified the structure of the fast waves in comparison with Figure 5. The Alfvén wave at $z = 0.5$ is just reaching the ionosphere at $t = 6$, and the diagnostic D_A (shown by a dashed-dotted line) is not large, and decreases with increasing x. This shows that at the lobe center where there is no Alfvén speed gradient the coupled Alfvén wave is close to being a pure Alfvén wave over much of its extent. We interpret the behavior at $z = 0.5$ in the same way as in AW and *Wright et al.* [1999]: They describe how the the dispersion diagram (Figure 2) may be used to predict the parallel wave number ($k_{\|A}$) for resonant fast and Alfvén wave coupling on each field line. Following this method (with $V_A(z = 0.5) = 1.0$) gives $k_{\|A}(z = 0.5) = 6.16$, or a parallel wave-

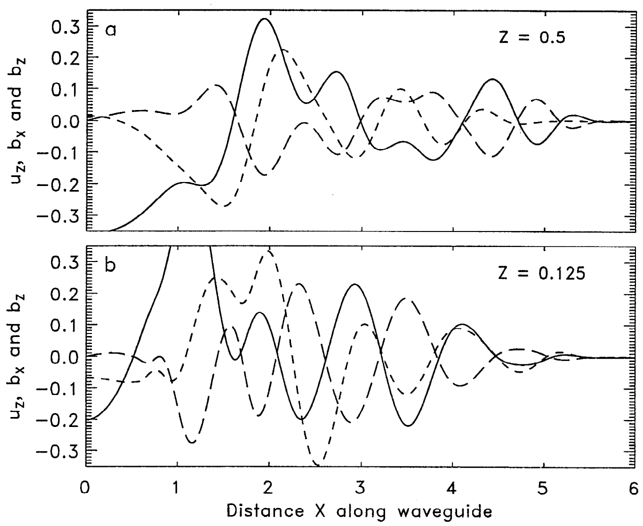

Figure 5. Field-aligned variation of the fast mode fields at $t = 6.0$ in the (a) lobe and (b) PSBL. Here u_z, b_x, and b_z are displayed as the solid, dashed, and long dashed lines, respectively ($t_d = 1.0$, $x_d = 0.48$, $k_y = 0.0$, so no Alfvén waves are excited).

length of 1.02 which is in good agreement with the value 1.05 measured directly off an enlarged copy of Figure 6. The parallel group velocity of the fast mode with $k_{\|} = k_{\|A}(z)$ is $V_{g\|}(k_{\|A}(z))$, which we write as $V_{g\|}(z)$ for brevity. For $n = 1$ and $z = 0.5$, $V_{g\|}(z)$ is found from Figure 2b to be 0.46. AW's interpretation is that of a slowly moving fast wave packet traveling at $V_{g\|}(z)$, which will have reached about $x = 3.25$ at $t = 6$ (allowing for time-of-flight and an initial pulse width of 0.48). Ahead of this wavepacket, an Alfvén wave is radiated which propagates at the local Alfven speed ($V_A = 1.0$).

The field line at $z = 0.125$ has $V_A(z = 0.125) = 0.842$, and with the aid of Figure 2 and the AW interpretation we predict $k_{\|A}(0.125) = 8.20$, so the parallel wavelength of the Alfven wave in Figure 6d should be 0.77 (in excellent agreement with the value measured directly from Figure 6 of 0.78). At $t = 6$ the resonantly driven Alfvén wave should have reached $x = 5.05$, while the fast mode radiating it propagates at $V_{g\|}(0.125) = 0.31$. Allowing for the inital driving condition extending to $x = 0.48$, we anticipate the driving fast mode component should have reached $x = 2.31$, and Figure 6 confirms that beyond this point D_A is small (indicating a predominantly Alfvénic perturbation). Note that although Alfvénic perturbations actually extend beyond $x = 5.05$, this portion of wave does not have the resonantly driven wavelength of the Alfvén wave in $x < 5.05$ and is probably driven nonresonantly by fast modes whose turning points lie at larger z.

Figure 7 is a stack plot of the structure of the velocity u_y associated with the Alfvén wave through the PSBL region. There is little change of u_y in the upper part of the PSBL. Below $z = 0.15$ the wavelength decreases rapidly, and there is a maximum of amplitude at about $z = 0.13$.

4.2. Model B

The slightly different z variation of Model B allows at least the first three fast harmonic dispersion relations of the waveguide to intersect the Alfvén continuum, as shown in Figure 3. The broader $k_{\|}$ spectrum of the initial impulse ($x_d = 0.24$) also provides significant power at larger $k_{\|}$. A stack plot of u_y through the PSBL region is shown for $t = 6$ in Figure 8. There is obvious harmonic structure which was lacking in the Model A results (see Figure 7).

Figure 9 shows the Fourier amplitude spectrum of the u_y structure at $z = 0.25$, the upper boundary of the PSBL where $V_A = 1$. Comparison with Figure 3a shows that the spectral peaks match well with the $k_{\|}$ values given by the intersections of the fast mode dispersion relations with the upper dashed $V_A = 1$ line at $k_{\|} = 3.64$, 9.91, and 15.90 (also indicated by the vertical dashed lines in Figure 9). This demonstrates that the three fast harmonics are driving three separate Alfvén waves on the single field line at $z = 0.25$. Generally, the intersection points of the $k_y = 0$ dispersion curves with the Alfvén continuum give extremely reliable estimates of the Alfvén wave harmonics that appear on field lines in the lobe and PSBL.

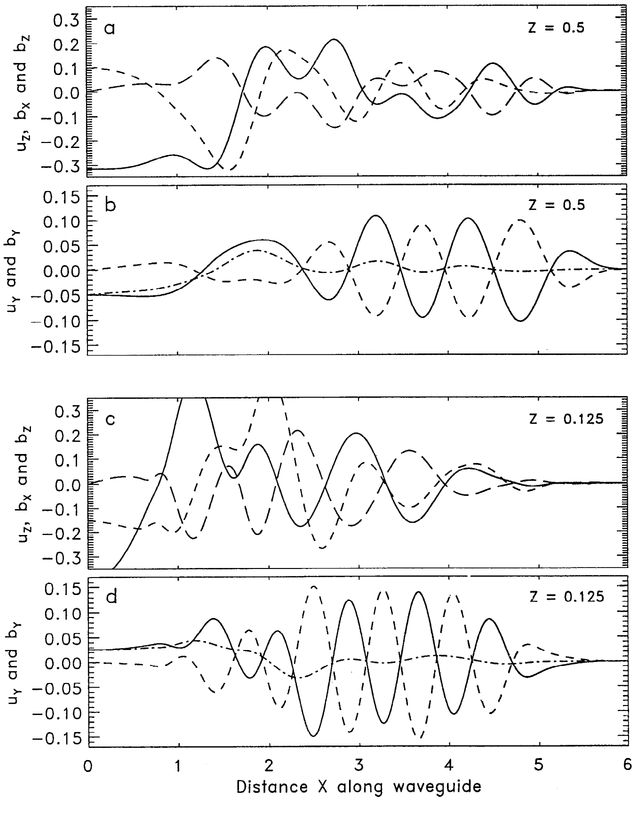

Figure 6. Similar to Figure 5, but with $k_y = 1.3$ so that Alfvén waves are excited. These are shown in Figures 6b and 6d. The Alfvén wave fields u_y and b_y are shown as solid and dashed lines, respectively. The dot-dash line is a plot of the Alfvén diagnostic (6) which is zero for a pure Alfvén wave propagating parallel to the equilibrium field.

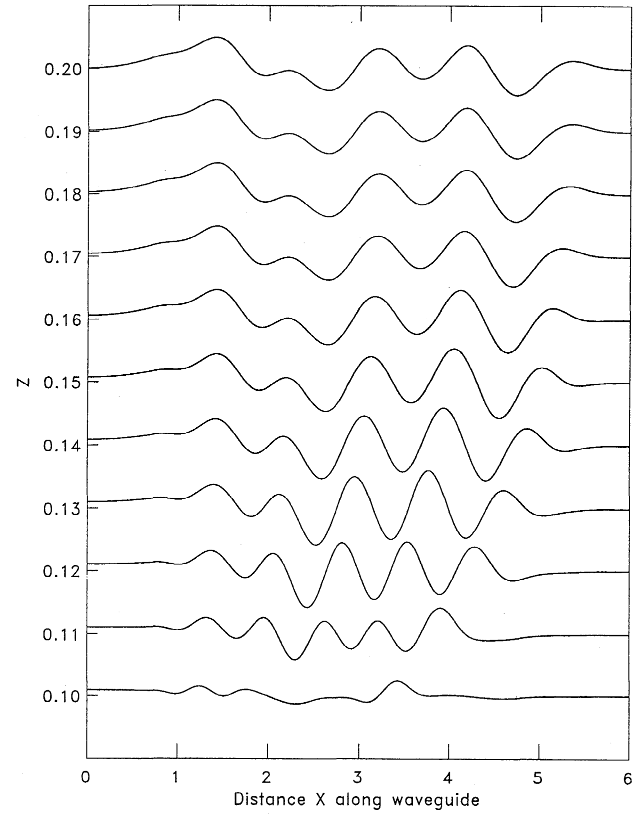

Figure 7. Stack plot of $u_y(x)$ for the parameters given in Figure 4 on field lines lying in the PSBL and beginning of the lobe. Model A was used.

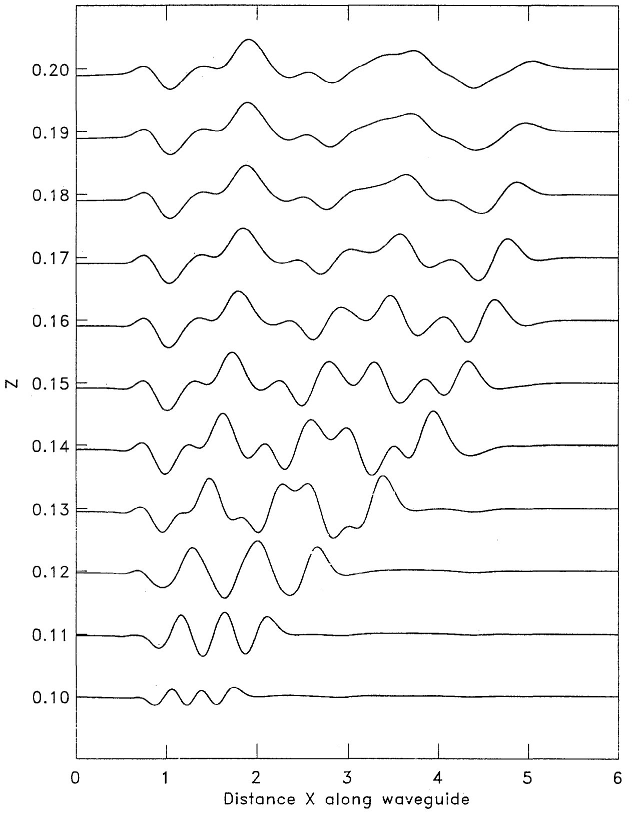

Figure 8. Similar to Figure 7, except $x_d = 0.24$, and Model B was used. Note the multiple harmonics present in the PSBL and lobe.

4.3. Model C

Model C incorporates the x variation in Figure 1c. The wave fields shown in Figure 10 are for $t = 6$ and $z = 0.125$ and can be compared with the fields in Figures 6c and 6d. As the waves travel into the region of increasing V_A (see Figure 1c) their wavelengths and propagation velocities increase, and they reach the ionosphere earlier than for Model A. These properties are as expected, and the Model C results appear to have no qualitative differences from those in Model A. Note that D_A is nonzero beyond $x \approx 5$. This is because the Alfvén wave fields here contain a component of Alfvén waves reflected from the ionosphere.

5. Discussion

5.1. Coupling Strength and k_y

In AW the value $k_y = 0.5$ was chosen to ensure that the coupling strength between fast and Alfvén waves was relatively weak. Here we have taken $k_y = 1.3$ as representing a realistic value for a fundamental mode structure across the magnetotail. As discussed earlier, the existence of significant Alfvén wave energy in the lobe suggests that $k_y = 1.3$ still represents relatively weak coupling. To test this, we show in Figure 11a the time development of the total fast and Alfvén wave energies in the model magnetotail. The slow increase of the Alfvén wave energy is exactly matched by the slow decrease in the fast mode energy, the total being constant to very good accuracy. However, the energy ratio in the bottom panel of Figure 11 is small, reaching only ~0.06 at $t = 9$, showing that coupling is still relatively weak for $k_y = 1.3$.

Although we only consider a single (small) k_y mode in our simulation, it is possible that a highly localized source in the tail could excite a broad k_y band. These modes would disperse in the y direction with small k_y components propagating only slowly in y. Thus extended Alfvén wave trains can only be excited by small

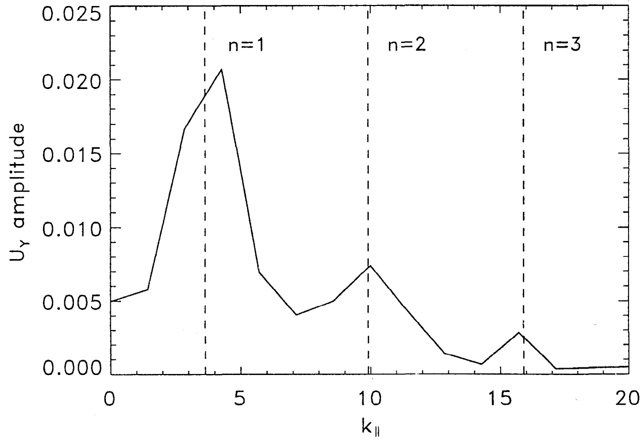

Figure 9. Fourier amplitude spectrum of u_y on the field line at $z = 0.25$ in Figure 8. The dashed lines show the $k_{\|}$ values for which the approximate theory predicts efficient coupling will occur.

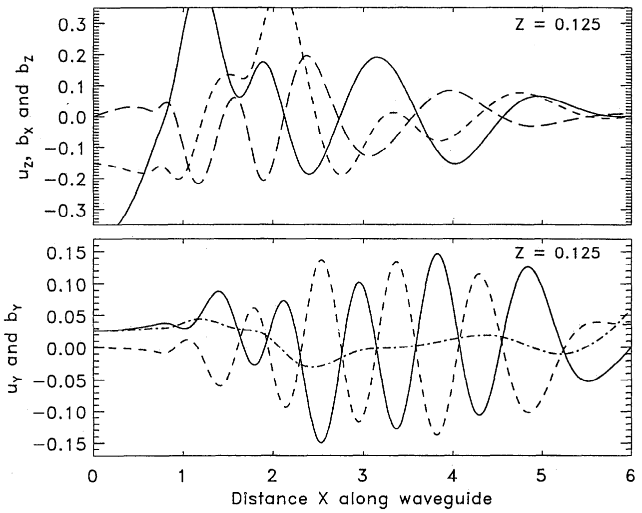

Figure 10. Similar to the two lowest panels in Figure 6, except that Model C was employed. (The Alfvén speed increases with x.) Comparing with the panels in Figure 6, we see that the Alfvén diagnostic is no longer zero for $z > 4.5$ as this region contains Alfvén waves reflected from the ionosphere.

k_y fast modes as they will stay on the field lines connected to the source region for many cycles, whereas larger k_y modes will propagate more quickly in y and not stay on any given field line for long. Since it is the small k_y fast modes that will drive Alfvén wave trains most readily, we expect our single small k_y calculation to give results that are a good guide to the Alfvén waves excited on field lines mapping to the source region. In the tail it is likely that only a small fraction of the fast mode energy will couple to Alfvén waves. The remainder will leak out of the magnetotail boundaries or be stored in a new equilibrium configuration.

5.2. Transverse Wave Number and Phase Velocity

From the contour plots in Figure 4 we see that the Alfvén wave in the lobe is essentially a plane wave propagating in the x direction, while the Alfvén wave in the PSBL rapidly phase mixes and therefore develops a significant transverse wave number k_z. We estimate k_z for Model A as follows. Parallel wavelengths were measured from large-scale plots of the last few cycles of the waves shown in Figure 7 and at intermediate z values. This was found to be more accurate than using Fourier transforms of the waves. The value of $k_{\|A}$ was determined through the PSBL at z increments of 0.005. Figure 12a shows a quartic polynomial that is an excellent fit to the measured values. Using this fitted function, the z variation of the Alfvén frequency is given by $\omega_A(z) = k_{\|A}(z)V_A(z)$, and is shown in Figure 12b.

The theory described by AW allows us to estimate $k_{\|A}(z)$ and $\omega_A(z)$ directly from the dispersion diagram (Figure 2). This was done for five representative positions throughout the PSBL, and the result is shown by the starred points in Figures 12a and 12b.

Equation (14) of AW gives the phase ϕ of the Alfvén wave as

$$\phi = k_{\|A}(z)x_0 - \omega_A(z)t_0, \tag{7}$$

where x_0 and t_0 are a given x position and time. The wave number k_z is then given by

$$k_z \simeq \partial\phi/\partial z. \tag{8}$$

For $t_0 = 6$ a representative position for the Alfvén waves in the PSBL is $x_0 = 4$. The resulting z variation of k_z is shown in Figure 12c. Finally, Figure 12d displays the phase velocity V_{pz} given by

$$V_{pz} = \omega_A/k_z. \tag{9}$$

Note that k_z is large and negative deep within the PSBL and becomes smaller as the lobe is approached. The ratio $|k_z/k_\||= 60$ for the smallest z value shown, and is zero in the lobe. V_{pz} is directed toward the plasmasheet, consistent with the equatorward propagating auroral waveforms discussed by *Wright et al.* [1999]. The extended theory developed in that paper (their equation (8)) also showed how k_z could be estimated as

$$k_z(x,z,t) \approx -k_{\|A}(z)\frac{dV_A}{dz}\frac{x - V_{g\|}(z)t}{V_A(z) - V_{g\|}(z)} \tag{10}$$

Here k_z is the local wavenumber on the field line at position z, a displacement x away from the source, and a time t following excitation. Again, $k_{\|A}(z)$ is the resonantly driven Alfvén wave field-aligned wavenumber at z, and $V_{g\|}(z)$ is the parallel group velocity of the fast mode exciting these Alfvén waves (i.e., $V_{g\|}(k_{\|A}(z))$), which may be read off the lower panel in Figure 2. The starred points in Figure 12 have z = (0.11, 0.13, 0.15, 0.17, 0.19), for which $V_{g\|}(z)$ = (0.265, 0.322, 0.396, 0.455, 0.462).

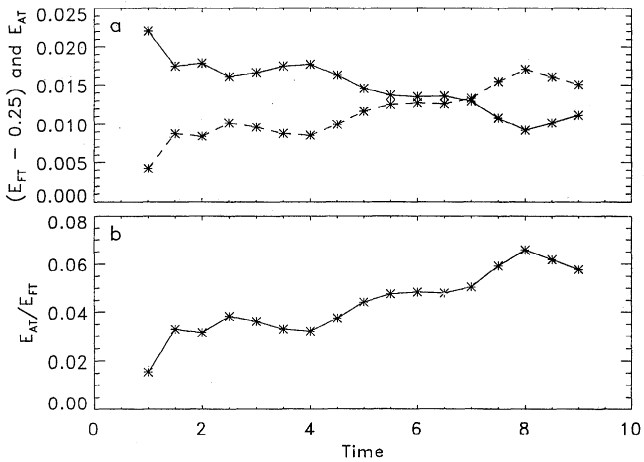

Figure 11. (a) The variation with time of the total fast and Alfvén wave energy densities integrated over the simulation domain ($E_{FT} - 0.25$ is shown by the solid line, and E_{AT} by the dashed line). (b) The relative variation. (Model A, $t_d = 1.0$, $x_d = 0.48$, $k_y = 1.3$).

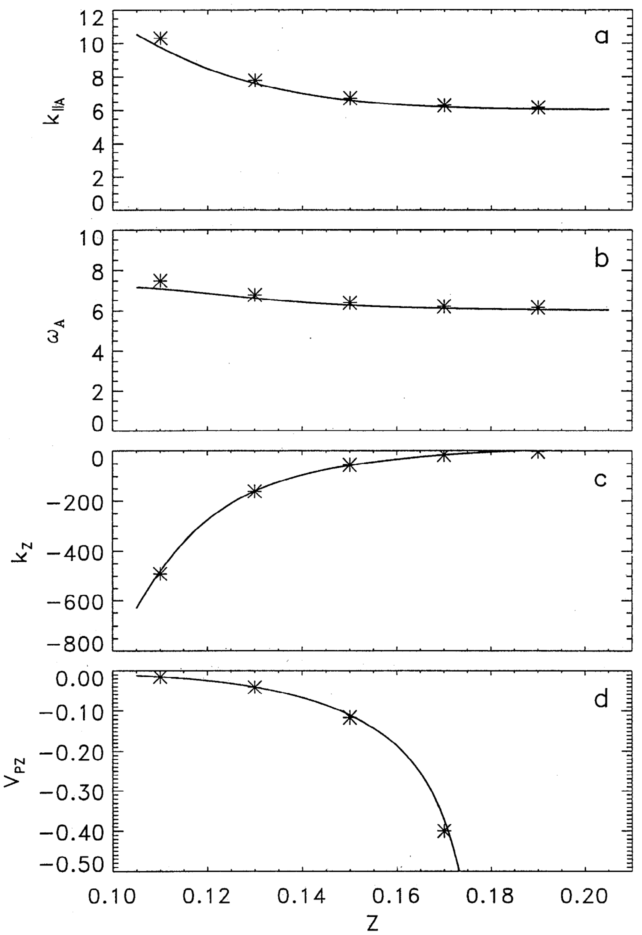

Figure 12. Alfvén wave parameters for the snapshot in Figure 4: (a) $k_{\|A}(z)$, (b) $\omega_A(z)$, (c) $k_z(z)$, and (d) $V_{pz}(z)$. The solid lines correspond to quantities estimated using the simulation results, while the starred points correspond to the predictions of the approximate theory.

The phase speed in z (V_{pz}) is then given by

$$V_{pz}(x,z,t) = \frac{-V_A(z)}{dV_A/dz} \cdot \frac{V_A(z) - V_{g\|}(z)}{x - V_{g\|}(z)t} \tag{11}$$

The theoretical predictions for k_z and V_{pz} are shown by the starred points in the lowest two panels of Figure 12. Evidently the theoretical predictions for the frequencies, wavenumbers and phase speeds of the resonantly driven Alfvén waves are in excellent agreement with the numerical values. (The agreement is within 5%, and generally much better than this.)

5.3. Parallel Current and Electric Field

The transverse wave number (k_z) shown in Figure 12 rapidly increases with time. This implies the development of a parallel current density given by the normalized relationship $j_\| = (\nabla \times \boldsymbol{B})_x$. Figure 13a shows the structure of $j_\|$ in the PSBL for model B at $t = 9$, after the wave has reflected from the ionosphere in the upper part of the PSBL. Figure 13b shows the developing spatial structure of $j_\|$ along the field line at $z = 0.135$. Note that there is essentially no parallel current in the lobe, as the Alfvén wave is locally independent of z there.

When k_z becomes comparable with the ion gyroradius ρ_i, kinetic effects become important, as discussed for example by *Hasegawa* [1976]. We have not yet included kinetic effects in the present model, but several general statements can be made about the consequences of doing so. With $k_z \sim \rho_i$ the phase mixed Alfvén wave becomes the so-called "kinetic Alfvén wave" [*Hasegawa,* 1976]. In the present case, this wave has a component of group velocity toward the central plasma sheet. The wave will quickly develop smaller transverse structure [e.g., *Johnson and Cheng,* 1997] and is likely to drive larger parallel current. We therefore expect that the $j_\|$ shown in Figure 13 should be a lower limit on the parallel current density when kinetic effects are included.

Another possibility is that a parallel electric field component may be generated when $k_z \sim \rho_i$ [*Hasegawa,* 1976]. The following expression for $E_\|$ is given by *Inhester* [1987] [see also *Hasegawa,* 1976].

$$E_\|/\rho^2 = \nabla_\| \nabla_\perp \cdot \mathbf{E}_\perp, \tag{12}$$

where $\rho = (T_e/m_i\Omega_i^2)^{1/2}$ is the thermal ion gyroradius for ions with the temperature T_e of the electrons, also known as the ion acoustic gyroradius. The ion mass and cyclotron frequency are m_i and Ω_i respectively. (12) is valid for $m_e/m_i < \beta \ll 1$, where m_e is the electron mass and β is the ratio of plasma pressure to magnetic pressure.

Figure 14a shows how the normalized $E_\|$ (given by the right-hand-side of (12) with ρ on the left-hand-side considered as a specified parameter) has developed in the PSBL for model B up to $t = 9$, and the middle panel shows the $E_\|$ structure along the $z = 0.135$ field

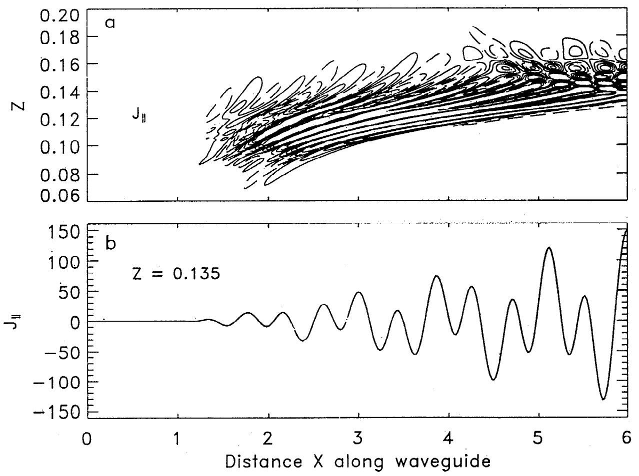

Figure 13. The field-aligned current density for Model B (x_d = 0.24, t_d = 1.0, k_y = 1.3) at t = 9.0: (a) a contour plot indicating the strongest current in the PSBL, and the presence of some waves reflected from the ionosphere. Positive values are denoted by solid contours, negative values by dashed contours. (b) The variation along the $z = 0.135$ PSBL field line.

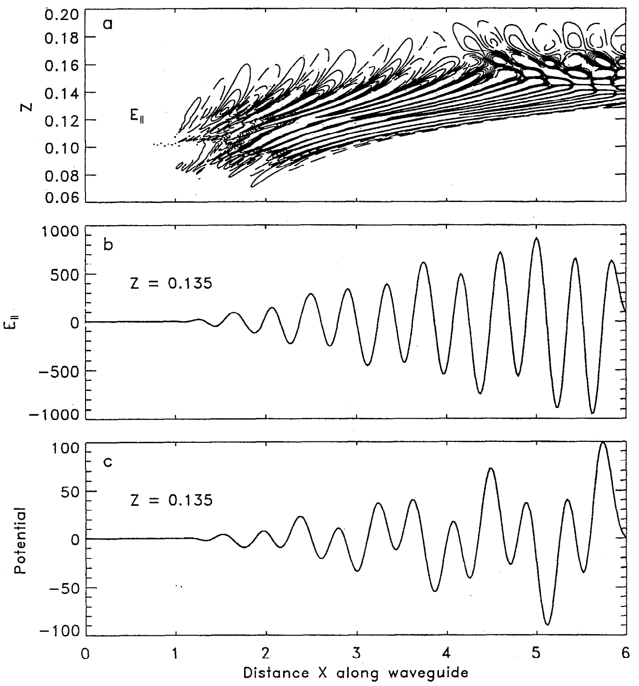

Figure 14. The variation of the parallel electric field with (a) x and z, and (b) along the $z = 0.135$ PSBL field line for the same parameters as in Figure 13. Positive values are denoted by solid contours, negative values by dashed contours. (c) The associated field-aligned potential.

line in the PSBL. Also shown in the bottom panel is the wave potential $-\nabla_\perp \cdot \mathbf{E}_\perp$ along $z = 0.135$. There is effectively no parallel electric field in the lobe.

The plasma sheet contains hot ions with $T_i > T_e$. Hot ion dispersive effects are likely to reduce $E_\parallel$ considerably [*Streltsov et al.*, 1998; *Cheng and Johnson*, 1999]. We should therefore take the $E_\parallel$ and potential shown in Figure 14 as being upper limits for values in the PSBL.

5.4. Implications for the Magnetosphere

To discuss how the results described above relate to the magnetosphere, we make the following physical parameter choices. We take the far tail lobe magnetic field to be $B_0 = 10$ nT and the lobe mass density to be 0.1 atomic mass units cm^{-3}, noting that cold O$^+$ beams exist in the lobe [e.g., *Mukai et al.*, 1994]. The Alfvén speed in the far tail lobe is then $v_2 = 700$ km s^{-1}. We also take the tail radius to be $z_0 = 25$ R_E. The electric field scale is then $E_0 = 7$ mV m^{-1} and the time unit is $v_2/z_0 = 227.5$ s, or ~4 min.

So far we have not dicussed an actual mechanism which may excite MHD waves in the tail. This has been done deliberately, since the wave propagation and coupling we have modeled is essentially the free response of the tail following a driving phase. The qualitative features of the response are largely independent of the driver. It is, perhaps, worth considering what events in the magnetotail could provide a suitable driver at this juncture. The obvious candidate is reconnection in the tail. In particular, the expulsion of a plasmoid will cause the overlying field lines to move in a manner that is qualitatively similar to our driver.

The spatial extent (x_d) and timescale (t_d) of our driver define a range of parallel wavenumbers and frequencies within which significant spectral power will lie. Crudely, we find most power in the bands $0 < \omega < 4\pi/t_d$ and $0 < k_\parallel < 2\pi/x_d$. These criteria may be viewed as bands in the ω–$k_\parallel$ dispersion diagrams, and modes lying where they overlap will be excited preferentially by the driver. Note that the equilibrium model determines the dispersion diagrams and the frequencies that we observe, while the driver represents a rather broad source which specifies which range of normal modes will have the most power.

The plasmoid parameters below are based upon the survey results reported by *Ieda et al.* [1998] for near tail and middle tail events. Typical plasmoids have an extent in x of $5-15$ R_E, which equates to $0.2-0.6$ in normalised units, and x_d values of $0.1-0.3$. These values are based upon the entry of the spacecraft into the plasmoid, and so may be a slight underestimate of the total plasmoid extent ($2x_d$). Thus our choice of $x_d = 0.24$ and 0.48 should represent typical plasmoid scales. We found smaller x_d could excite several Alfvén harmonics on a single field line, while plasmoids with larger x_d are likely to excite just one harmonic. The number of harmonics excited may be estimated by comparing the Fourier envelope and the dispersion diagrams (Figures 2 and 3), and this may provide a useful diagnostic of both x_d and the equilibrium tail structure.

Spacecraft measurements of plasmoid signatures have a duration of $1-2$ min. This is normally the interval the spacecraft spends inside the plasmoid. Hence the total time it takes a plasmoid to convect past a spacecraft could be more like $2-4$ min. Thus our choice of $t_d = 1.0$ (equivalent to 4 min) is again typical of plasmoids. The total extent of a plasmoid in z is $8-15$ R_E, so the typical maximum z displacement of the northern overlying field lines will be ~6 R_E, and this will occur over a time $t_d/2$. Thus the amplitude of u_z for the overlying field lines is 320 km s^{-1}. This is about half of our lobe Alfvén speed, and since we used a normalised driving velocity of unit amplitude we must scale all the fields by a factor of a half when calculating the dimensional magnetospheric

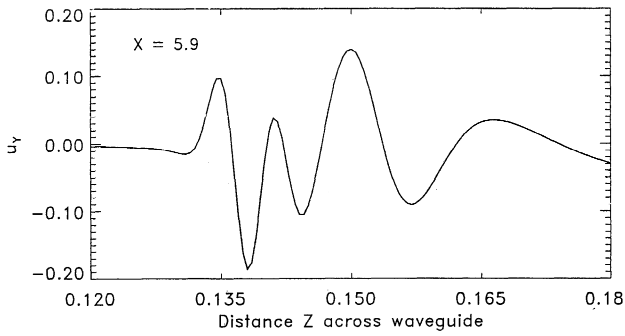

Figure 15. The variation of u_y across the PSBL for Model B at $t = 9.0$.

fields predicted by our model. In Figure 6 for Model A the Alfvén wave amplitudes in the lobe become $u_y = 35$ km s^{-1} ($E_x = 0.35$ mV m^{-1}) and $b_y = 0.5$ nT. The PSBL values are $u_y = 50$ km s^{-1} ($E_x = 0.5$ mV m^{-1}) and $b_y = 0.8$ nT.

From Figure 12 we find that for Model A at $x = 4$ the Alfvén wavelength in the lobe is about 25 R_E, while that in the inner PSBL is $\sim$ 15 R_E. The Alfvén wave frequency in the lobe is 4.2 mHz, and in the inner PSBL it is 5 mHz. The maximum k_z in the inner PSBL implies a transverse wavelength of 2200 km, and the transverse phase velocity there is $V_{pz} \simeq 20$ km s^{-1}.

In this simplified model, the vicinity of the ionosphere at $x = 6$ can be thought of as the region where the geomagnetic field begins to become dipolar. Mapping of our results to the auroral zone and polar cap can only be through approximate mapping factors until a model with a more detailed structure is developed. If we assume that the inner PSBL maps to the high-latitude auroral zone, a z length in the PSBL is reduced by a factor of $\sim$40 when mapped to the ionosphere, and a transverse area is reduced by a factor of the order of 10^3.

Using a mapping factor of 40, the equatorward wave phase velocity at the auroral ionosphere is $\sim$0.5 km s^{-1}, consistent with that derived from the observed waveforms discussed by *Wright et al.* [1999]. The frequencies of 4 to 5 mHz described above are also reasonably consistent with observations, although somewhat larger than generally observed.

For the Model B PSBL in Figure 13b the largest current density shown corresponds to $j_{\|} = 3 \times 10^{-9}$ A m^{-2}. The area mapping factor of 10^3 means that wave field-aligned current densities at the auroral ionosphere are $\sim 3 \times 10^{-6}$ A m^{-2}, consistent with the observations of *Walker et al.* [1992]. Kinetic effects (discussed in section 5.3) may increase $j_{\|}$ in the PSBL even further. However, the Alfvén waves in the lobe carry no significant field-aligned current.

The parallel electric field in Figure 14 requires a value for the ion acoustic gyroradius. If we make the reasonable choices $T_e = 5 \times 10^6$ K and a PSBL magnetic field of 7 nT, then ρ is $\sim$300 km. The corresponding maximum $E_{\|}$ in Figure 7 is 0.01 mV m^{-1}, which is small but not negligible. The last peak in Figure 14c corresponds to a potential difference between that x position and the ionosphere of $\sim$200 V. Because the potential is oscillatory in x, this means that particles could only be accelerated to a maximum energy of 200 eV before reaching the ionosphere. As discussed in section 5.3, these $E_{\|}$ and energy values are likely to be upper limits because of hot ion kinetic effects in the PSBL. Therefore particle energization by the wave $E_{\|}$ in the PSBL is likely to be negligible compared with the required 10 keV energies of observed auroral particles.

Figure 15 shows the structure of u_y across the PSBL for Model B at $x = 5.9$ and $t = 9$. The minimum scale size in z of the Alfvén waves at this point is $\sim$1000 km. A mapping factor of 40 gives a scale size of 25 km at the auroral ionosphere, and kinetic effects in the PSBL may make this scale size even smaller.

At a distance of the order of 5 R$_E$ above the ionosphere the waves pass the transition point between finite gyroradius dominance and finite electron inertia dominance [e.g., *Lysak and Carlson,* 1981; *Streltsov and Lotko,* 1995]. The dispersive properties of the waves are reversed as they become electron inertial Alfvén waves, and it is possible for a significant $E_{\|}$ to exist. This $E_{\|}$ strongly depends on the size of the perpendicular wavenumber k_z. If k_z is already large because of phase mixing and kinetic effects in the PSBL, then large values of $E_{\|}$ could develop, giving significant particle energization. Inclusion of kinetic effects in the present model is required to investigate this possibility.

Note that transverse wavelengths in the PSBL for Model A are much larger than likely values of ρ. Kinetic effects in the PSBL will therefore be too small to reduce the transverse wavelength significantly, and subsequent inertial effects will also be negligible. Model A can therefore explain the latitudinal wavelengths and equatorward phase velocities of the oscillating auroral structures discussed by *Liu et al.* [1995] and *Wright et al.* [1999]. However, it cannot directly explain the particle energization giving rise to the observed auroral luminosity. It is possible that there is some unseen fine wave structure superimposed on the large-scale wave that leads to particle acceleration in the inertial region, or that the large-scale wave is modulating particles energized elsewhere. It may be significant in this context that the PSBL phase-mixed Alfvén waves carry large field-aligned current and are associated with auroral luminosity, while the lobe plane Alfvén waves carry no field-aligned current, and no oscillating auroral structures have been reported in the lobe region of the ionosphere. Note that there is weaker phase mixing in the mantle region (see Figure 4), and the Alfvén waves there have poleward phase velocities.

The lobe/polar cap system is not devoid of interest, however. *Wright et al.* [1999] suggested that once Alfvén waves begin to be reflected from the ionosphere they will have the local structure of a standing Alfvén wave. *Allan* [1993] showed that a standing Alfvén wave with a realistic amplitude in a dipole field could generate a significant nonlinear ponderomotive force (PMF). The PMF depends strongly on the L value, and quasi-standing waves in the polar cap would exist on field lines with effectively very large L values. The resulting PMF could extract ionospheric O$^+$ ions and accelerate them to energies of at least several hundred eV, providing a possible source for the cold ion beams commonly observed in the far tail lobes [e.g., *Mukai et al.*, 1994]. Our results show that only relatively small values of k_y allow the existence of significant lobe Alfvén wave amplitudes, since fast modes with larger k_y will not penetrate the lobe. PMF extraction of ionospheric O$^+$ could only occur when k_y has these small values.

6. Conclusions

Our numerical simulations of MHD waves in the Earth's magnetotail indicate that the natural response of the tail to fast mode driving is to couple energy into

Alfvén waves in the PSBL and the lobe, and to a lesser extent in the mantle. Detailed features of the Alfvén waves produced in the simulations (such as frequency, field-aligned wave number, phase-mixing length, and phase velocity) are shown to be predicted very reliably using the $k_y = 0$ dispersion diagrams and the approximate theory developed by *Allan and Wright* [1998] and *Wright et al.* [1999].

The Alfvén waves excited on a given field line are dependent upon the length-scale and timescale of the driver, as this determines the area in $(\omega, k_\parallel)$-space of the dispersion diagram where there is significant energy. It was shown that by altering the $k_\parallel$ spectrum of the driver, several Alfvén harmonics could be excited on a single field line. Thus the simple observation of Alfvén oscillations from a spacecraft in the tail along with a model of the equilibrium can be used to constrain the possible dimensions of the energy source via the dispersion diagram.

The PSBL has the strongest phase mixing of Alfvén waves. This appears to account for the equatorward phase motion of observed relatively large-scale oscillating auroral structures. However, the associated auroral particle energization is not directly explained by the model. Strong field-aligned currents are generated in the PSBL, and for larger PSBL Alfvén speed gradients kinetic effects are likely to be important. The lobe Alfvén waves do not phase mix and remain as plane waves. It is not expected that lobe Alfvén waves will be associated with optical emissions, but it is suggested they may accelerate ionospheric ions into the distant tail lobe.

Acknowledgments. The authors are grateful to both referees for very useful comments, and to Chris Owen for helpful discussions. W.A. was partially supported by the New Zealand Foundation for Research, Science and Technology through contract CO1627. A.N.W. is supported through a U.K. PPARC Advanced Fellowship.

The Editor thanks Dong-Hun Lee and another referee for their assistance in evaluating this paper.

References

Allan, W., Plasma energization by the ponderomotive force of magnetospheric standing Alfvén waves, *J. Geophys. Res., 98,* 11,383, 1993.

Allan, W., and A. N. Wright, Hydromagnetic wave propagation and coupling in a magnetotail waveguide, *J. Geophys. Res., 103,* 2359, 1998.

Brillouin, L., *Wave Propagation and Group Velocity,* Academic, San Diego, Calif., 1960.

Cheng, C. Z., and J. R. Johnson, A kinetic-fluid model, *J. Geophys. Res., 104,* 413, 1999.

Elphinstone, R. D., et al., The double oval UV auroral distribution, 1, Implications for the mapping of auroral arcs, *J. Geophys. Res., 100,* 12,075, 1995.

Goertz, C. K., and R. A. Smith, The thermal catastrophe model of substorms, *J. Geophys. Res., 94,* 6581, 1989.

Hasegawa, A., Particle acceleration by MHD surface wave and formation of aurora, *J. Geophys. Res., 81,* 5083, 1976.

Herron, T. J., An average geomagnetic power spectrum for the period range 4.5 to 12,900 seconds, *J. Geophys. Res., 72,* 759, 1967.

Ieda, A., et al., Statistical analysis of the plasmoid evolution with Geotail observations, *J. Geophys. Res., 103,* 4453, 1998.

Inhester, B., Numerical modeling of hydromagnetic wave coupling in the magnetosphere, *J. Geophys. Res., 92,* 4751, 1987.

Johnson, J. R., and C. Z. Cheng, Kinetic Alfvén waves and plasma transport at the magnetopause, *Geophys. Res. Lett., 24,* 1423, 1997.

Liu, W. W., B.-L. Xu, J. C. Samson, and G. Rostoker, Theory and observation of auroral substorms: A magnetohydrodynamic approach, *J. Geophys. Res., 100,* 79, 1995.

Lysak, R. L., and C. W. Carlson, Effect of microscopic turbulence on magnetosphere-ionosphere coupling, *Geophys. Res. Lett., 8,* 269, 1981.

McClay, J. R., and H. R. Radoski, Hydromagnetic propagation in a theta-model geomagnetic tail, *J. Geophys. Res., 72,* 4525, 1967.

Mukai, T., M. Hirahara, S. Machida, Y. Saito, T. Terasawa, and A. Nishida, Geotail observations of cold ion streams in the medium distance magnetotail lobe in the course of a substorm, *Geophys. Res. Lett., 21,* 1023, 1994.

Pulkkinen, T. I., D. N. Baker, C. J. Owen, and J. A. Slavin, A model for the distant tail field: ISEE 3 revisited, *J. Geomagn. Geoelectr., 48,* 455. 1996.

Samson, J. C., T. J. Hughes, F. Creutzberg, D. D. Wallis, R. A. Greenwald, and J. M. Ruohoniemi, Observations of a detached, discrete arc in association with field line resonances, *J. Geophys. Res., 96,* 15,683, 1991.

Samson, J. C., D. D. Wallis, T. J. Hughes, F. Creutzberg, J. M. Ruohoniemi, and R. A. Greenwald, Substorm intensifications and field line resonances in the nightside magnetosphere, *J. Geophys. Res., 97,* 8495, 1992.

Streltsov, A. V., and W. Lotko, Dispersive field line resonances on auroral field lines, *J. Geophys. Res., 100,* 19,457, 1995.

Streltsov, A. V., W. Lotko, J. R. Johnson, and C. Z. Cheng, Small-scale, dispersive field line resonances in the hot magnetospheric plasma, *J. Geophys. Res., 103,* 26,559, 1998.

Walker, A. D. M., et al., Spatial and temporal behavior of ULF pulsations observed by the Goose Bay HF radar, *J. Geophys. Res., 97,* 12,187, 1992.

Wright, A. N., Dispersion and wave coupling in inhomogeneous MHD waveguides, *J. Geophys. Res., 99,* 159, 1994.

Wright, A. N., W. Allan, R. D. Elphinstone, and L. L. Cogger, Phase mixing and phase motion of Alfvén waves on tail-like and dipole-like magnetic field lines, *J. Geophys. Res., 104,* 10,159, 1999.

Xu, B.-L., J. C. Samson, W. W. Liu, F. Creutzberg, and T. J. Hughes, Obervations of optical aurora modulated by resonant Alfvén waves, *J. Geophys. Res., 98,* 11,531, 1993.

Yamamoto, T., K. Shiokawa, and S. Kokubun, Magnetic field structures of the magnetotail as observed by Geotail, *Geophys. Res. Lett., 21,* 2875, 1994.

Zalesak, S. T., Fully multidimensional flux-corrected transport algorithms for fluids, *J. Comput. Phys., 31,* 335, 1979.

W. Allan, National Institute of Water and Atmospheric Research, P. O. Box 14-901, Kilbirnie, Wellington, New Zealand. (e-mail: w.allan@niwa.cri.nz)

Andrew N. Wright, Mathematical Institute, University of St. Andrews, St. Andrews, Fife KY16 9SS, Scotland. (e-mail: andy@dcs.st-and.ac.uk)

(Received February 19, 1999; revised August 10, 1999; accepted September 14, 1999.)